THESIS FOR THE DEGREE OF LICENTIATE OF ENGINEERING

Multiscale modelling of total pressure effects on complete methane oxidation over Pd/Al_2O_3

Carl-Robert Florén

CHALMERS

Department of Chemistry and Chemical Engineering
Division of Applied Chemistry
Competence Centre of Catalysis
CHALMERS UNIVERSITY OF TECHNOLOGY
Gothenburg, Sweden 2018

Multiscale modelling of total pressure effects on complete methane oxidation over Pd/Al_2O_3

CARL-ROBERT FLORÉN

Licentiatuppsatser vid Institutionen för kemi och kemiteknik
Chalmers tekniska högskola
Nr 2018-16

Department of Chemistry and Chemical Engineering
Division of Applied Chemistry
Competence Centre for Catalysis
Chalmers University of Technology
SE-412 96 Gothenburg
Telephone +46 31 772 1000

Typeset in LaTeX
Printed by Chalmers Reproservice
Gothenburg, Sweden 2018

Multiscale modelling of total pressure effects on complete methane oxidation over Pd/Al_2O_3

CARL-ROBERT FLORÉN
Department of Chemistry and Chemical Engineering
Chalmers University of Technology

Abstract

The models used in heterogeneous catalysis are becoming more advanced and the literature shows an increased interest in incorporating the atomistic scale into microkinetics. Coupling kinetics based on first-principles calculations to macroscopic effects can pave the way towards more comprehensive modelling methods and to tailored catalyst designs. The theme of this thesis is to couple a reaction model based on first-principles to mass and heat transport and develop a multiscale reactor model for complete methane oxidation. The multiscale model is used to determine if the activity of an alumina supported palladium catalyst can be enhanced by increasing the reaction total pressure. First, a 1D porous catalyst model is developed where the kinetics and mass and heat transport are discussed for complete methane oxidation over Pd/Al_2O_3 for a simulated exhaust gas. It is shown that the catalyst performance can be enhanced by increasing the total pressure. However, the positive effect is constrained by a high coverage of the hindering surface species bicarbonates, adsorbed water and hydroxyl groups originating from the water and carbon dioxide in the bulk gas. The reaction controlling phenomenas are identified for a range of temperatures and total pressures. Next, a 2D multiscale reactor model is developed to predict methane conversions. The conversion can be increased if the temperature is sufficiently high to overcome the desorption barriers of surface species hindering dissociative methane adsorption. The effects of total pressure on surface kinetics, and mass and heat transport are discussed.

Keywords: methane oxidation; palladium oxide; multiscale modelling; reactor modelling; mass and heat transport; first-principles calculations

List of Publications

This thesis is based on the following appended papers:

I. Modelling complete methane oxidation over palladium oxide in a porous catalyst using first-principles surface kinetics
C-R. Florén, M. Van den Bossche, D. Creaser, H. Grönbeck, P-A. Carlsson, H. Korpi, M. Skoglundh
Catalysis Science & Technology, 2018, **8**, 508-520

II. Multiscale reactor modelling of total pressure effects for complete methane oxidation on Pd/Al_2O_3
C-R. Florén, P-A. Carlsson, D. Creaser, H. Grönbeck, M. Skoglundh
In manuscript

My Contributions to the Publications

Paper I

I wrote the script for the porous washcoat model, performed all the calculations, wrote the first draft of the manuscript and finalised the paper together with my co-authors.

Paper I

I wrote the script for the multiscale model, performed all the calculations, wrote the first draft of the manuscript and finalised the paper together with my co-authors.

Contents

Chapter 1

Introduction

At the moment of writing, the Earth's popluation is 7.5 billion and increases with 1.2 % per year [1, 2]. The increased number of people increases the challenge of striving for sustainable development where we can share and effectively use the limited amount of resources. This increases the necessity for more energy efficient and more environmentally friendly energy conversion technologies, agricultural processes and transportation systems in our society. In 2014 it was reported that the energy, agriculture, industry and transportation sectors are the biggest contributors of released of anthropogenic carbon dioxide (CO_2) [3]. The energy and transportation sectors make up for about two-thirds of the anthropogenic global carbon dioxide emissions and hence can act as key players in the problem of global warming. Most of the released CO_2 is reported to originate from the energy sector while the transportation and industry sectors are the second and third most important sources for CO_2 emissions [3, 4]. Both sectors have traditionally used fossil fuel sources for energy conversion processes. To counter the increasing release of greenhouse gases (GHG) several global initiatives have been started. Two well-known initiatives are the Kyoto protocol, which was signed in 1997, and the EU 2020 strategy, where the goal was to reduce GHG by 20 % by the year of 2020, relative to 1990 [5, 6]. The main GHGs include CO_2, methane (CH_4), nitrogen oxides (NO_x), and chlorofluorocarbons (CFC) [7, 8]. While each of them are causing global warming, their relative potentials are different and commonly it is measured by carbon dioxide equivalents. For example, methane has a global warming potential of about twenty times that of carbon dioxide [9]. The largest sources of released methane into the atmosphere include oil and gas extraction, waste treatments, agricultural systems and fuel combustion [10, 11]. Since methane has a strong global warming potential it

is preferable to convert the released methane into carbon dioxide and hence reduce the environmental impact.

A long-term global strategy to reduce the environmental footprint is to shift the focus from using fossil fuels into more sustainable energy sources with low environmental impact. Two fuel sources that has regained interest is natural and biogas which both consist primarily of methane. The gases can be used within the energy and the transportation sectors and substitute the more polluting fuels based on crude oil and coal of today used in gas turbines and combustion engines. Compared to petrol and diesel, combustion of natural gas benefits from reduced CO_2, NO_x, sulfur oxides (SO_x) and soot emissions [12]. The reduced CO_2 release is attributed the short CH_4 hydrocarbon molecule with the lowest carbon-to-hydrogen ratio of all hydrocarbons. For every combusted methane molecule only one CO_2 is formed. As a comparison, the corresponding number of formed CO_2 from diesel is roughly ranging from ten to twenty, depending on the raw material and manufacturing process [13]. However, since CH_4 is a potent GHG it is important to remove any traces of methane slip through the gas turbine or combustion engine. The methane slip can favorably be processed by an abatement system and converted into CO_2 and water. For methane abatement, generally a palladium based catalytic aftertreatment system is chosen for its favorable properties towards complete methane oxidation. In the complete methane oxidation reaction the CH_4 is oxidised into CO_2 and water. Further, traditionally an aluminum oxide supported palladium catalyst (Pd/Al_2O_3) is used to catalyze the complete methane oxidation reaction.

1.1 Thesis objectives

The primary purpose of this thesis is to investigate how the performance of a porous Pd/Al_2O_3 catalyst for complete oxidation of methane is affected by the total pressure. The thesis describes a new multiscale model, based on first-principles calculations, which is used to evaluate the effects of varying reaction conditions. In Paper I a 1D catalyst model is developed and the effects of adding mass transport to first-principles based reaction kinetics is discussed in the porous Pd/Al_2O_3 catalyst. In paper II, the model is upgraded into a 2D reactor model. The reactor is given the geometry of a monolith which is commonly used in applications. The 2D reactor model is used in paper II to simulate methane conversion and evaluate the axial gradients and kinetics

inside a monolith for complete methane oxidation at varying temperatures and total pressures.

Chapter 2

Natural gas applications

2.1 Energy conversion and transportation fuel

Natural gas and biogas are comparable in their composition and combustion properties. Both fuel sources consist primarily of methane (CH_4) with a dry methane content of around 90 and 60 %, respectively [14–17]. Biogas typically has a lower methane content and a higher carbon dioxide and SO_2 content, depending on its production process. However, biogas can preferably be upgraded into biomethane after removing the impurities hydrogen sulfide (H_2S), CO_2 and moisture. Biomethane is comparable to natural gas and can use the natural gas infrastructure [18, 19]. Even though it today exists advanced technologies for heat and power generation, i.e. gas turbines, and engine designs for maximal efficiency, uncombusted methane slips through. The high GHG potential of methane makes it essential to remove any traces which otherwise ends up in the atmosphere. The methane slip can be managed by a catalytic converter which has proved to be a successful technology for exhaust cleanup applications. Depending on the application and whether the technology operates under rich (fuel excess) or lean (oxygen excess) condistions the catalyst must be designed for the specific application to display and maintain its performance over time. Rich conditions can preferably be used for the partial oxidation reaction and syngas production, where the products of interest are hydrogen and carbon monoxide. Syngas can be used for chemical synthesis and as an energy source for gas burners and electricity generation. Lean conditions, on the other hand, are of interest when dealing with combustion processes and the complete methane oxidation reaction, where the formed products are water and carbon dioxide.

Common applications are heat and electricity generation and power generation in internal combustion engines like diesel, petrol and dual-fuel engines. However, methane being the shortest hydrocarbon chain is a stable molecule and difficult to catalytically oxidise at the lower temperatures found in vehicle applications. The arguments motivate further research on the methane oxidation reaction in search for more efficient and better performing catalytic materials.

2.2 Heterogeneous catalysis

Catalysis is present everywhere and enables many things that are taken for granted. The photosynthesis and the metabolism in our bodies are just two examples. Both are examples of important catalytic processes where the former enables vegetation to use CO_2, water and light to synthesise biomass and the latter to convert glucose into CO_2, water and heat in our cells. If the catalyst and the reactants are in different phases, the process is categorised as heterogeneous catalysis. Heterogeneous catalysis is widely used in the production of, e.g., fuels, chemicals, fertilizers and utilised in emission control systems to remove unwanted components. Inventions such as synthetic fuel and rubber, automotive exhaust aftertreatment systems and fuel cell technology are examples of applications of heterogeneous catalysis.

The activation energy of a chemical reaction is the minimum potential energy required for the reactants to undergo chemical transformation. The activation energy varies in magnitude depending on the nature of the reaction and the reaction conditions. Therefore, in some reactions high temperature and pressure are necessary for a specific reaction to take place. A catalyst provides an alternative reaction pathway with a lower activation energy but without being consumed itself as illustrated in Figure 2.1. The catalyst thus offers a less energy demanding and faster reaction rate than compared to the corresponding non-catalysed reaction. Importantly, the thermodynamic properties of the overall reaction are not altered, hence a catalyst has no effect on a reaction that is inherently thermodynamically unfeasible.

A generic heterogeneous catalytic reaction is illustrated in Figure 2.2. First off all the reactants, A and B, must be transported from the bulk gas to the outer boundary of the catalyst surface (external diffusion). From the surface A and B are transported into the porous catalyst structure and to the vicinity of an active site (internal diffusion). At

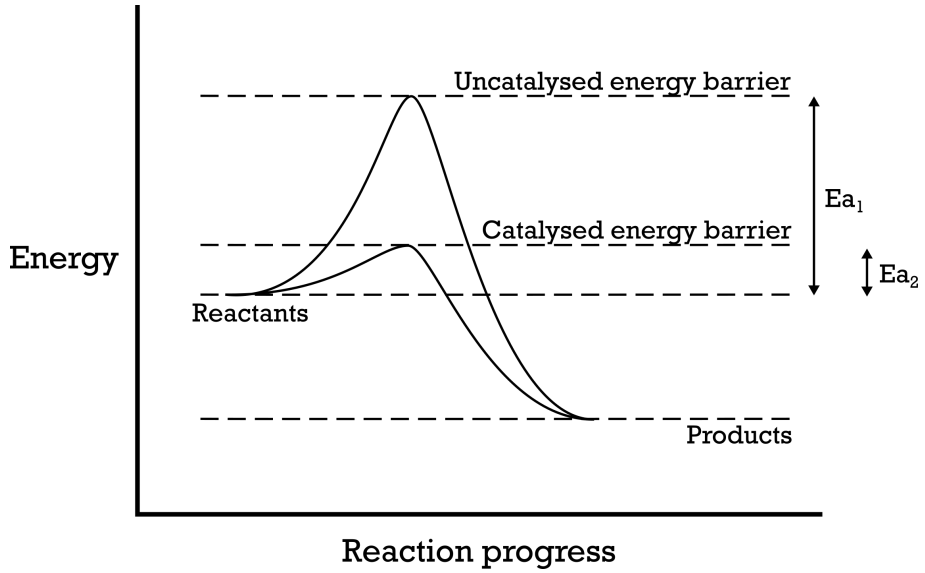

Figure 2.1: An illustration showing the basic principle of catalysis. The energy barrier for the uncatalysed reaction (Ea_1) is higher than the corresponding energy barrier for the catalysed reaction (Ea_2). The latter is made possible by using a catalyst that offers a more energy effective reaction mechanism.

the active site molecule A, and/or B depending on the reaction mechanism, bonds to active site (adsorption) where it reacts into product C (surface reaction). At this point, C has to break its bonds to the active site (desorption) and be transported from the porous structure to the surface boundary (internal diffusion) and ultimately from the surface outwards and into the bulk gas (external diffusion). The overall reaction process, here converting A and B into C, is only as fast as the slowest subprocess which can be either one of the steps 1-7 in Figure 2.2. The slowest step is the bottleneck of the reaction and is referred to the rate-limiting or rate determining step.

In practice there exists a large variety of catalyst and reactor designs to optimise the considered reaction rate. Two common but different catalyst designs are zeolites, which benefit from a well-defined microporous structure with few irregularities, metal oxide supported catalysts which are simple to manufacture but are amorphous solids which lack any long-range order in their structure. Which one is being used is often a question of application and tradition and it cannot be said that either one is better than the other. Apart from the catalyst design, the actual reactor in which the catalyst is held, can be designed in various ways to optimise the reaction conditions around and inside the catalytic material. This optimisation includes many parameters, for example

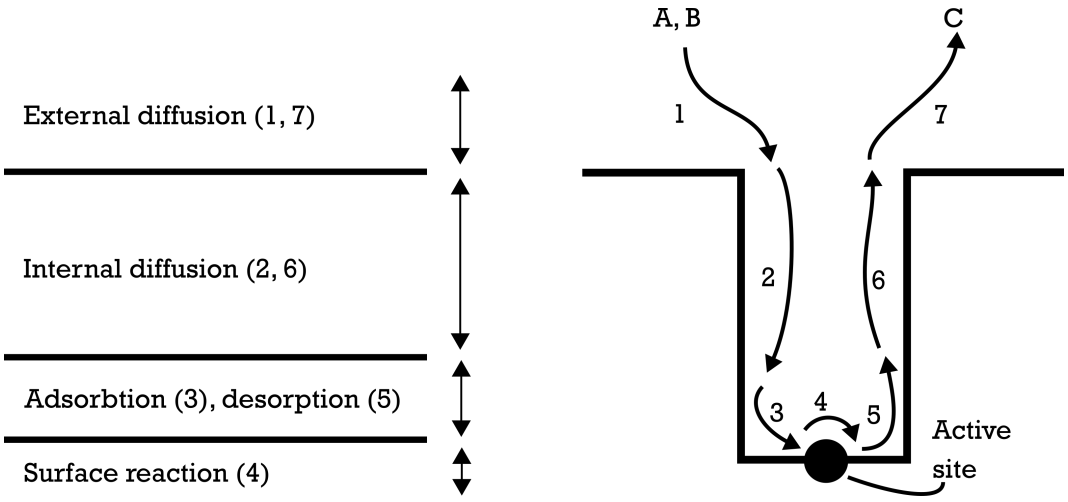

Figure 2.2: Illustration of the different steps of catalysed reaction over a solid particle in a porous support. The slowest step is called the rate-limiting or rate determining step.

geometry of reactor vessel, internal packing material, flow characteristics and more. These will not be discussed further here. The interested reader is encouraged to read [20] to get an overview of reactor design.

Efficient use to achieve high conversion and selectivity from the catalyst is dependent on the reaction conditions, such as gas composition, temperature and total pressure, which can vary over the surface and inside the porous catalyst as well as being time dependent. Therefore process monitoring and control are vital to maintain favorable reaction conditions. Catalytic reactions can in many cases demonstrate an increased performance when operated at elevated pressures. Two examples are the oxidative steam reforming of methane, where steam is used to produce hydrogen gas, and combustion of methane for power generation [21–24]. Currently, however, the literature is scarce at low temperatures, which is relevant for vehicle emission abatement, and high pressures.

2.3 Complete methane oxidation

The overall chemical reaction for complete oxidation of methane is shown in equation 2.1. Following the stoichiometry, one methane molecule is oxidised into one carbon dioxide and two water molecules. The reaction is highly exothermic with a reaction enthalpy of -802 kJ/mole which means that energy is released as methane is combusted.

The autoignition temperature for the complete methane oxidation is experimentally reported to be around 750 °C [25] whereas by using a catalyst, ignition temperatures closer to 300 °C can be achieved. Traditionally platinum or palladium supported on metal oxides are used to catalyse the complete oxidation of methane reaction.

$$CH_4 + 2O_2 \rightleftharpoons CO_2 + 2H_2O \tag{2.1}$$

$$\Delta H_r = -802.3\ kJ/mole$$

These metals can catalyse the dissociation of the symmetric and stable methane molecule [26–30]. Alumina (Al_2O_3), ceria (CeO_2), silica (SiO_2) and zirconia (ZrO_2) or combinations of these are common support materials for the application [31–35]. The Pd/Al_2O_3 catalyst has been shown to exhibit a high activity for complete methane oxidation at lower temperatures. Many studies have been devoted to identify the nature of the active site of palladium at varying reaction conditions. In lean (oxygen rich) conditions an oxidised state of palladium, PdO, has been reported to possess the high catalytic activity [36–38]. Furthermore, the most active surface to dissociatively adsorb the methane molecule is reported to be PdO(101) [37–40]. The PdO(101) surface is illustrated in Figure 2.3 using a ball-and-stick model.

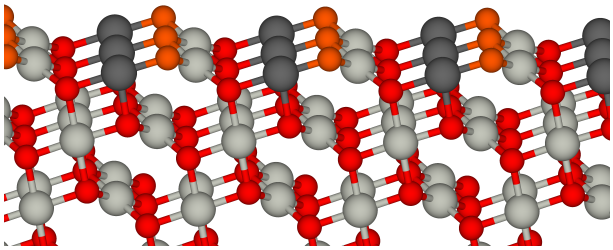

Figure 2.3: A ball-and-stick model of the PdO(101) surface. Here black is a threefold coordinated Pd, orange is a threefold coordinated O while gray and red are the fourfold coordinated arrangements of Pd and O, respectively [41].

Despite showing high activity for methane oxidation, Pd/Al_2O_3 catalysts are unfortunately cursed by a low tolerance towards sulfur and water [42–44]. These compounds impair the catalytic activity by blocking of the active sites and affecting the support structure. Sulfur is present in trace amounts in the fuel. The content varies with production method and source. Water, being a reaction product of combustion of methane,

can inevitably be removed for the exhaust gas without installing an additional separation unit after the combustion process. Therefore further research is required to find and produce active methane oxidation catalysts with maintained performance under reaction conditions. Furthermore, obtaining atomistic knowledge about the methane oxidation reaction coupled to mass and heat transport phenomena in the catalyst could offer a comprehensive understanding of the overall reaction rate. The combination pave the way for new methods of analysing the catalytic systems. This kind of models, based on first-principles calculations, can be used to identify whether the bottleneck is within the intrinsic reaction rate or if mass and heat transport processes are controlling the studied reaction. Once the controlling phenomenon is identified, an optimization procedure can reveal new ideas and methods for catalyst design and preparation. These complex models require significant computational efforts but with more efficient methods and better resources available today, the calculations can reveal better performing catalytic structures and reaction conditions by tailoring the catalyst for the application.

Chapter 3

Multiscale reactor modelling

Ideally we want to understand a chemical process down to its core mechanism and describe reactions through first-principles calculations without using fitting parameters. This can be achieved with multiscale modelling which refers to a type of modelling where a considerable number of different time and length scales are coupled within the same model. Since multiscale modelling raises the complexity of an already complex system it requires significant computational efforts. The method has seen many developments the last decades as better computers and more efficient algorithms have become available.

3.1 Reactor modelling

The reactor model in this thesis is considered to be a continuous flow reactor and behave as a plug flow reactor (PFR). In a PFR the differential volume of bulk gas flow through the reactor is assumed to move as a uniform plug, i.e. axial dispersion of the gas phase is assumed to be negligible. The tanks-in-series method is used to discretize the reactor in its length scale, which is of common practice. The tanks-in-series method assumes each reactor segment to behave as an ideal tank reactor where all the fluid properties are uniform within each tank.

The continuous flow reactor possesses a monolithic reactor geometry. The governing mass balance through the monolithic reactor in axial flow direction (x) and in radial direction (z), i.e. perpendicular to the axial direction, is

$$\frac{\partial F_i}{\partial x} - \Gamma_i \cdot \frac{\partial C_i}{\partial z} = 0 \tag{3.1}$$

where F_i is the bulk molar flow rate for gas component i, C_i is the gas phase concentration. Γ is here a lumped mass transport coefficient where equimolar counter diffusion is assumed to prevail from the bulk gas and into the porous catalyst.

The governing adiabatic heat transport equation in axial and radial direction is

$$\frac{\partial F_i}{\partial x} \cdot C_p \cdot (T_f - T_g) - h \cdot A_s \cdot (T_g - T_s) = 0 \tag{3.2}$$

where C_p is the heat capacity of the bulk gas, T_f is the feed temperature, T_g is the bulk gas temperature, h is the heat transport coefficient, A_s is the surface area open to heat transport between the catalyst surface and the bulk gas and T_s is the catalyst surface temperature. Equation 3.1-3.2 describe the axial variations in the bulk gas and a similar set of equations is needed to consider internal mass and heat transport. Internal transport refers to the mass and heat transport inside the catalyst in a radial direction. The internal mass balance is

$$\Gamma \cdot \frac{C_i}{\partial z} + \int_{z=0}^{z=L_{wc}} \nu_i \cdot r_i \cdot c_{site} \cdot m_{cat} = 0 \tag{3.3}$$

where ν is the stoichiometric coefficient, r is the reaction rate determined from first-principles microkinetics, c_{site} is the active site density and m_{cat} is the mass of the catalyst. Since the catalyst material often is a good heat conductor, the catalyst in considered to be isothermal in the radial direction throughout this thesis. The assumption is motivated by the Anderson's criterion [45]. Heat transport is present between the catalyst surface and bulk gas, and in the axial direction. The corresponding heat balance is

$$h \cdot A_s \cdot (T_g - T_s) - A_{c.s} \cdot (q_{k,in} - q_{k,out}) + \int_{z=0}^{z=L_{wc}} r_i \cdot m_{cat} \cdot C_{site} \cdot (-\Delta H_r) \cdot \partial z = 0 \tag{3.4}$$

where $A_{c.s}$ is the cross sectional area of the porous catalyst between tanks, q_k is the solid heat flux between tanks and ΔH_r is the reaction enthalpy.

Heat conduction between tanks is described according to

$$q = -2 \cdot \lambda_s \cdot \frac{T_s}{\partial x} \tag{3.5}$$

where q is the heat flux inside the monolith in axial direction and λ_s is the catalyst heat conductivity. The thermal radiation from both ends of the channel is accounted for

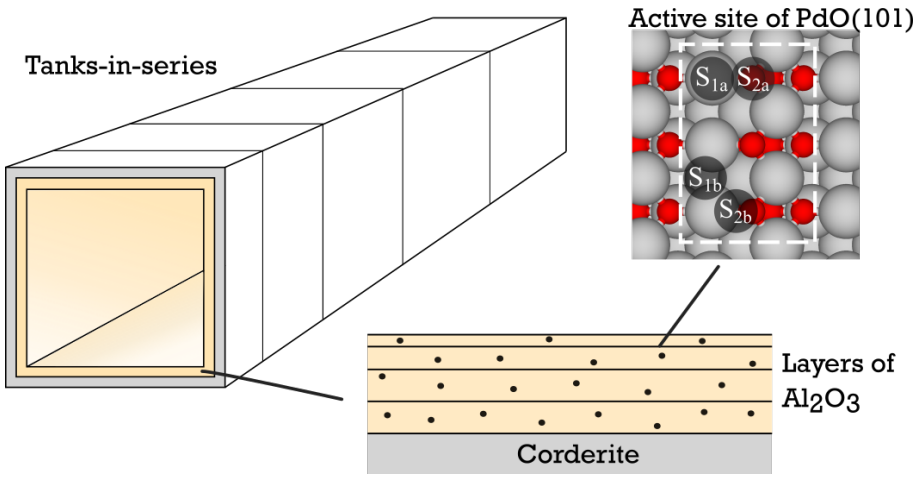

Figure 3.1: An illustration of the discretised monolith reactor. The shown number of tanks and layers do not correspond to the number used by the model.

according to eq. 3.6.

$$q = \epsilon \cdot \sigma \cdot (T_s^4 - T_g^4) \tag{3.6}$$

where ϵ is the emissivity factor and σ is the Stefan-Boltzmann constant. Equations 3.1-3.5 are discretised by dividing the reactor into tanks and catalyst layers in order to solve them numerically and obtain axial (along monolith) and radial (in porous catalyst) gradients. The monolith is simulated as a single-channel reactor model. The single-channel monolith is divided into 10 tanks, according to the tanks-in-series method, while the porous catalyst is divided into 12 layers to account for internal mass and heat transport. The length of the tanks and the thickness of the layers increases with 30% from the inlet and 50% from the catalyst surface, respectively, to obtain a finer gradient resolution. An illustration of the reactor model is shown in Figure 3.1. The active site density, c_{site}, is back-calculated from a desired noble metal loading and dispersion in each tank and layer. The active site density is calculated in each tank and layer to obtain an even site distribution inside the catalyst.

3.1.1 Calculating transport coefficients

Some explanation of the lumped mass transport coefficient in eq. 3.1 is necessary. It has already been mentioned that it assumed that equimolecular counter diffusion prevails in radial direction. This assumes that the diffusion of the different gas species balances each other out and the net rate of molar diffusion is zero. There is hence no molar

accumulation in the porous catalyst. Through this assumption and by setting up the mass balances between bulk gas and catalyst surface, and between catalyst layer n and layer n+1, a lumped mass transport coefficient, Γ, for component i, tank k and layer n (n=0 denotes the bulk gas) can be expressed as

$$\Gamma_{i,k,0} = \frac{A_k}{\frac{1}{k_{c,i}} + \frac{0.5\Delta z_1}{D_{eff\ i,n}}} \tag{3.7}$$

$$\Gamma_{i,k,n} = \frac{A_k}{\frac{0.5\Delta z_n}{D_{eff\ i,n}} + \frac{0.5\Delta z_{n+1}}{D_{eff\ i,n}}} \tag{3.8}$$

where A_k is the surface area of the catalyst open to mass and heat transport in tank k, $k_{c,i}$ is the mass transport coefficient from bulk gas to the catalyst surface for component i and Δz is the thickness of the catalyst layer n. The effective diffusivity, $D_{eff,i,k}$ is the effective diffusion coefficient for component i in tank k. The effective diffusion is estimated from the Bosanquet relation

$$D_{eff,i,k} = \frac{\epsilon_p/\tau}{\frac{1}{D_{i,k}} + \frac{1}{Dk_{i,k}}} \tag{3.9}$$

where ϵ_p/τ is the ratio of porosity to tortuosity and set to 0.1 [46, 47]. $D_{i,k}$ is the temperature and total pressure corrected bulk diffusion coefficient. Dk_i is the Knudsen diffusion coefficient which includes the structural parameter of pore width. The diffusion coefficients are calculated as

$$D_i = D_{ref,i}(\frac{T_s}{T_{ref}})^{1.75}(\frac{P_{ref}}{P_{tot}}) \tag{3.10}$$

$$Dk_i = \frac{d_p}{3}\sqrt{\frac{8R_gT_s}{M_i\pi}} \tag{3.11}$$

where $D_{ref,i}$ is taken from literature values, T_s is the catalyst surface temperature, d_p is the pore diameter and M_i is the molecular mass of component i. The physical parameters of $k_{c,i}$ and h_k, the mass and heat transport coefficients respectively, are heavily affected by the flow characteristics (i.e. laminar or turbulent flow). In turbulent flows, mass and heat transport are faster than in corresponding laminar flows. There are different was to calculate or estimate the coefficients, one would be to incorporate computational fluid dynamics (CFD) to solve the Navier-Stokes equation. CFD is commonly used to follow a developing flow field through a predefined control system and

can yield accurate results even for complex systems. The drawback is its high computational demand and the requirement of an experienced user to correctly describe the flow. Since the same reactor geometries have been used frequently in both research and industry over many years, a simple and fast method of calculating the transport coefficients by using dimensionless numbers has been developed. The dimensionless Sherwood and the Nusselt numbers, relate the fluid properties of mass and heat transport, respectively. The Sherwood and Nusselt numbers can then be used to calculate the mass and heat transport coefficients if the diffusion coefficient and thermal conductivity are known. The generic Sherwood and Nusselt numbers are

$$Sh = \frac{k_c L}{D_i} = \frac{Convective\ mass\ transfer}{Diffusion\ rate} \tag{3.12}$$

$$Nu = \frac{h_k L}{\lambda_g} = \frac{Convective\ heat\ transfer}{Conductive\ heat\ transfer} \tag{3.13}$$

where L is the characteristic lenght for a given geometry and λ_g is the thermal conductivity of the bulk gas. Equations 3.12-3.13 are valid for a fully developed laminar flow field and do not take into account the effects of turbulence on the transport coefficients k_c and h_k.

3.1.2 Mass and heat transport coefficients in a monolith

One of the simpler concepts of reactor designs would be a packed bed reactor where the feed enters the reactor vessel and has to circumvent a catalytically active packing material. The packing material can have many different shapes and be made of different materials such as ceramic or metallic raschig rings and pall rings [20]. The simplest packing is to fill the reactor with irregular shaped catalytic particles straight from the manufacturer. However, this would result in an unwanted and high pressure drop over the reactor due to the tight packing of small particles. This phenomenon is strongly dependent on the reactor geometry and catalyst structure. A monolith geometry benefits from a much lower pressure drop compared to a packed bed reactor and can thus handle high flows. As the fluid moves through the monolith a developed laminar flow profile is created. For a fully developed laminar flow the Sherwood and Nusselt numbers have converged to their asymptotic values of 2.98 [48]. The flow field is least developed in the beginning of the monolith which increases the transport coefficients in that area.

As a laminar fluid profile is developed through the monolith the Sherwood and Nusselt numbers converge to their asympthotic values. A common way to describe these variations in the flow is to use the Hawthorn's correlations for mass and heat transport between the bulk gas and the catalyst surface [49].

$$k_{c,i} = Sh_a \cdot \frac{D_i}{dh} \cdot (1 + \frac{0.095 \cdot Re \cdot Sc \cdot dh}{\sum_{j=1}^{k} \Delta x_j - 0.5\Delta x_k})^{0.45} \tag{3.14}$$

$$h_k = Nu_a \cdot \frac{\lambda_g}{dh} \cdot (1 + \frac{0.095 \cdot Re \cdot Pr \cdot dh}{\sum_{j=1}^{k} \Delta x_j - 0.5\Delta x_k})^{0.45} \tag{3.15}$$

where Re is the Reynold number, Sc is the Schmidt number, Pr is the Prandtl number and Δx is the tank segment length of the discretized monolith.

3.2 First-principles microkinetic reaction rate

A comprehensive multiscale reactor model requires that the reaction rate is expressed through first-principles calculations to include the atomistic scale. The reaction term in equations 3.3-3.4 is thus described by a microkinetic reaction mechanism based on Density functional theory (DFT) and its kinetics is described by Transition state theory (TST). In this section the basic background theory of developing a first-principles microkinetic reaction model is described.

3.2.1 Identifying the reaction landscape

The electrons and their interactions with surrounding protons and electrons are what give rise to different observable phenomena and properties such as reactivity, magnetism and whether a material is an insulator or a good conductor. It is thereby not difficult to accept that electron movement is crucial in catalysis where their movements give rise to the reaction at hand. DFT has become a more common tool in physics and chemistry to describe molecular structures that are a result of their electron configurations. The Schrödinger equation describes the total energy for an atomistic system according to

$$\hat{H}\Psi = E\Psi \tag{3.16}$$

where $\hat{H}$ is the Hamiltonian and describes the total energy of the system and E are the eigenvalues for the quantified energy levels. The solution of the equation Ψ is the wave function describing the motion of the electrons in the examined quantum system. Unfortunately, the Schrödinger equation only has an analytical solution for a one-electron system and lack an exact solution for many-body systems. Due to the lack of analytical solutions for all but the hydrogen atom, some assumptions are required. As mentioned, Equation 3.16 describes the quantum system as a set of wave functions. Already in 1927, when Thomas and Fermi introduced the idea, the electron densities have been used instead of their wave functions [50, 51]. The theorem translates the wave functions into electronic densities, $\rho(\mathbf{r})$ but was first proved in 1964 by Hohenberg and Kohn [52]. One year later, a method was developed by Kohn and Sham to evaluate the electron density [53]. By separating E in eq. 3.16 into terms of external potential, classical Coulomb interaction (here called Hartree) and a kinetic term, the energy can be expressed as

$$E = E_{ext}[\rho] + E_{Hartree}[\rho] + E_{kin}[\rho] \tag{3.17}$$

Further, the kinetic term can be separated into a non-interaction term (where the particles do not feel each other) and a term denoted the exchange-correlation functional.

$$E = E_{ext}[\rho] + E_{Hartree}[\rho] + T_{non-int}[\rho] + E_{xc}[\rho] \tag{3.18}$$

Since all terms but the exchange-correlation functional consider independent particles, the resulting equation is relatively simple compared to the original many-body system. The simplification is popular when using DFT where the challenge comes from evaluating E_{xc}. Its exact format is not known but methods based on different assumptions have emerged to evaluate its effects. Common methods are the local density approximation, generalized gradient approximations and hybrid functionals [54]. Their exact appearance and use will not be covered in this thesis. In practice, DFT is used to solve equations 3.16 and 3.18 with a chosen approximation for the exchange-correlation term. From the solution that describes the electron densities, an energy landscape and possible arrangement of molecules can be identified. The energy landscape describes the energy of the considered system as a function of a real-space coordinate. On top of the energy landscape possible reaction pathways, with a reactant state and a product

state, can be identified and evaluated in terms of how prone they are to bond to the surface.

3.2.2 Calculating the rate constants

Now an energy landscape has been determined for the catalytic surface and possible reactants and products have been identified. All that remains is to describe the transition between the reactant and product state, and its kinetics. Transition state theory (TST) is a methods saying that a reaction step between reactant state (R) and product state (P) progresses through a transition state ($TS^{\ddagger}$), which lies at a saddle point on the energy landscape between R and P [55, 56]. This can be illustrated as

$$R \longleftrightarrow TS^{\ddagger} \rightarrow P \tag{3.19}$$

The states R and $TS^{\ddagger}$ are assumed to be in equilibrium while the transition from state $TS^{\ddagger}$ to state P is irreversible. The rate of which P is produced, k^{TST} can be expressed as

$$k_{TST} = \frac{k_B T}{h} \frac{Z^{\ddagger}}{Z^R} e^{\frac{-\Delta E}{RT}} \tag{3.20}$$

where k_b is Boltzmann's constant, h is Planck's constant, T is the temperature, ΔE is the electronic energy barrier between $TS^{\ddagger}$ and R, and Z denotes the partition function for the respective state. The partition functions, Z, can be written as a product of the separable partition functions of translational, rotational and vibrational energies ($Z = Z_{trans} \cdot Z_{rot} \cdot Z_{vib}$). Of the separable partition functions, the vibrational partition function is most cumbersome since the vibrational frequencies of each mode are required. The vibrational frequencies are often obtained through a harmonic oscillation approximation and calculated from the DFT calculations.

Activated adsorption events with activation energy E_a are here described by the kinetic gas theory and its kinetics are described by

$$k_{ads}^{TST} = \frac{S_0 S_{dyn} A_{site}}{\sqrt{2\pi m k_B T}} e^{\frac{-E_a}{RT}} \tag{3.21}$$

where S_0 is the sticking coefficient accounts for the entropy change upon adsorption, S_{dyn} an additional sticking coefficient accounting for the fact that a molecule has

to approach the surface in a favorable orientation in order to adsorb, A_{site} is the area per adsorption site and m is the mass of adsorbed molecule.

3.2.3 Obtaining reaction rates

When the temperature dependent reaction constants have been identified it is possible to compile the considered elementary steps describing the reaction mechanism. Take the following reaction as an example where the reactants A and B are converted into the product C.

$$A_2(g) + B(g) \longleftrightarrow C(g) \tag{3.22}$$

Assume the reaction proceeds via a Langmuir–Hinshelwood mechanism where the reactants are first adsorbed onto neighboring sites before the surface reaction occurs. The elementary steps describing the reaction are written as

$$A_2(g) + 2* \longleftrightarrow 2A^* \tag{a}$$

$$B(g) + * \longleftrightarrow B^* \tag{b}$$

$$A^* + B^* \longrightarrow C(g) + 2* \tag{c}$$

Then the time dependent coverage of surface species A and B are expressed as

$$\frac{\partial \Theta_A}{\partial t} = 2k_a^+ \Theta_*^2 - 2k_a^- \Theta_A^2 - k_c^+ \Theta_A \Theta_B \tag{3.23}$$

$$\frac{\partial \Theta_B}{\partial t} = k_b^+ \Theta_* - k_b^- \Theta_B - k_c^+ \Theta_A \Theta_B \tag{3.24}$$

where $k_i^{\pm}$ is the rate constant for elementary reaction i and * denotes an empty site. Equations 3.23-3.24 can be solved numerically to obtain a steady state (time independent) solution by setting the left hand side of the equations equal to zero. In the same way a general expression for a large number of elementary steps can be formulated as

$$\frac{\partial \Theta_i(t)}{\partial t} = \sum_i (\nu_{ij} r_i(\Theta_1, ..., \Theta_N)) \tag{3.25}$$

where $\Theta_i(t)$ is the coverage of surface species i at time t and ν_{ij} is the stoichiometric coefficient for species i and reaction j. Equation 3.25 is solved for steady state reaction rates and coverages in each tank and catalyst layer in the reactor model. The reaction rates are used in equations 3.3 and 3.4 by the multiscale model to describe the reaction rate inside the catalyst at given gas condition and temperature.

3.2.4 Analysing surface kinetics

A common method to analyse surface kinetics is to correlate the turnover frequency (TOF) to the coverage of species on the catalyst surface. The latter is helpful to determine whether certain surface intermediates or byproducts are affecting the catalyst performance by blocking active sites. Another way of evaluating the kinetics is to determine the so called degree of rate control. The degree of rate control analysis is powerful when the most important elementary steps or reaction pathways are searched for. The rate control is a measure of the influence of elementary step *i* on the reaction rate while keeping the equilibrium constant fixed [57]. The degree of rate control is determined according to Eq 3.26.

$$\chi_i = \frac{k_i}{r}\left(\frac{\partial r}{\partial k_i}\right)_{K_i} \tag{3.26}$$

where (χ_i) is the degree of rate control, k_i is the surface reaction rate constant for reaction step i, r is the calculated turn over frequency from the microkinetic model and K_i is the equilibrium constant for reaction step i.

Chapter 4

Complete methane oxidation

This chapter stretches common modelling boundaries of complete methane oxidation and discusses the results obtained from the outlined multiscale model. The reader is reminded that the main objective of this thesis is to investigate the total pressure effects on complete methane oxidation. This thesis is based on the results from the two studies presented in Paper I-II. In paper I, a first-principles microkinetic model for complete methane oxidation on PdO(101), developed by M. Van Den Bossche [58], is coupled to mass and heat transport processes in a 1D porous catalyst layer given the physical properties of Al_2O_3. The considered microkinetic elementary steps are shown in Table A.1-A.3 in Appendix. The effects of transport processes are assessed by varying the total pressure and temperature. In Paper II the gained experience is used to upgrade the 1D catalyst model into a 2D multiscale monolith reactor model.

4.1 Porous catalyst modelling

In Paper I the performance of complete methane oxidation on a fully dispersed 2 wt.-% Pd/Al_2O_3 catalyst is simulated in a 1D porous catalyst. The model is described by the equations in chapter 3.1 but omits the axial variation described by equations 3.1 and 3.2. The simulations are performed for a typical exhaust gas composition containing 1000 vol.-ppm CH_4, 10 vol.-% O_2, 5 vol.-% H_2O and 5 vol.-% CO_2. The thickness of the porous catalyst is set to 100 μm which is a reasonable thickness in monolith applications while the pore diameter is set to 13 nm. The bulk gas is in this study considered to possess a fully developed laminar flow profile, i.e. Sh and Nu are fixed at 2.98. It is shown that the turnover frequency of complete methane oxidation in a porous catalyst

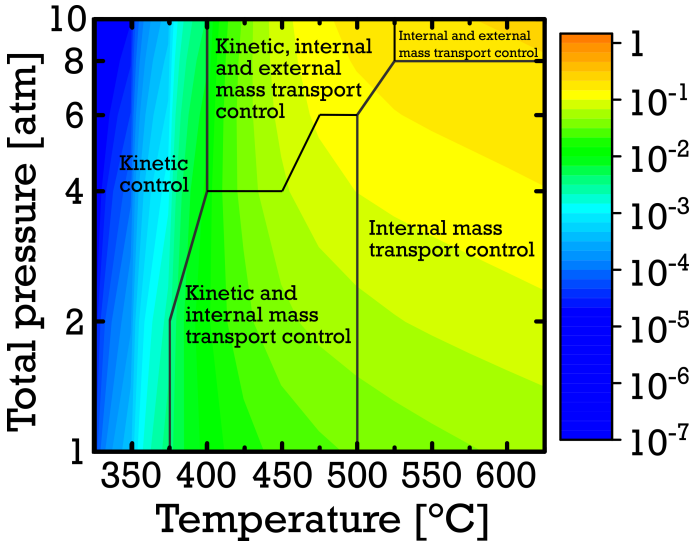

Figure 4.1: The turnover frequency and reaction controlling phenomena for complete methane oxidation in a 100 μm thick porous Pd/Al_2O_3 catalyst layer for varying temperatures and total pressures at a simulated exhaust gas composition of 1000 vol.-ppm CH_4, 10 vol.-% O_2, 5 vol.-% H_2O and 5 vol.-% CO_2 and Ar as balance.

can be considerably enhanced by increasing the total pressure but requires temperatures of 450 °C. At the same time, an increased total pressure can be detrimental to the catalytic activity if the temperature is lower than 400 °C. The turnover frequency and the reaction controlling phenomena are shown as a function of temperature and total pressure in Figure 4.1. The underlying factors giving rise to the different total pressure dependencies are attributed to the coverage of bicarbonate, adsorbed water and hydroxyl groups. Bicarbonates are formed through a surface reaction where adsorbed carbon dioxide reacts with a hydroxyl group while surface hydroxyl is formed from decomposition reactions of CH_4 and adsorbed water. The inhibitory effects of bicarbonate and water on palladium based methane oxidation catalysts have been reported by others [24,59,60]. The coverages of bicarbonate, adsorbed water, hydroxyl groups and free Pd-O site pairs are shown in Figure 4.2. At higher temperatures, where increasing the total pressure has a positive effect on the activity, it is observed that the catalyst surface is relatively free from the hindering bicarbonate, adsorbed water and hydroxyl groups. According to the microkinetic model the hindering surface species are adsorbed on the undercoordinated Pd atom and hence hinder further methane dissosiation by blocking the active sites. A higher temperature is therefore necessary to overcome the desorption barriers of the hindering species

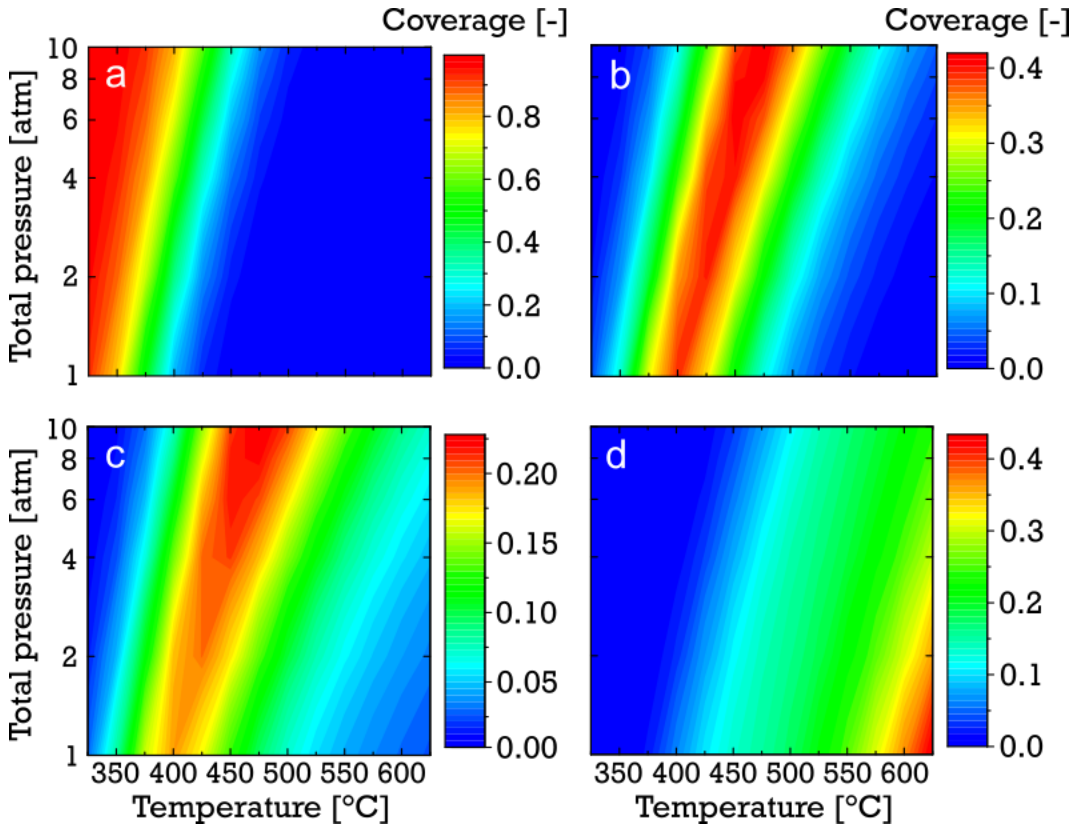

Figure 4.2: Equilibrium coverages of bicarbonate (a), water (b), hydroxyl (c) and free Pd–O site pairs (d) on S1 sites on PdO for complete CH_4 oxidation.

It was shown in Paper I that transport processes do have a significant effect on the observed TOF of methane oxidation in a porous catalyst at the examined reaction conditions. The catalyst is considered to be isothermal according to the Anderson's criterion. For an exothermic reaction, a slow heat transport from the catalyst surface to the bulk gas has a positive effect on the reaction rate since the exothermic heat is contained inside the catalyst. At the examined conditions, the temperature increase is found to be highest at high temperatures and total pressures, where the TOF is the highest and the most reaction heat is generated. The heat transport effects together with the prevailent mass transport effects strongly affect the observed TOF. The reaction controlling phenomena shown in Figure 4.1 are determined through comparing the external and internal time constants to the reaction time constant. The ratios are called the external and internal transport significance, respectively, and are often used to evaluate the influence of internal and external transport. The temperature difference between bulk gas and catalyst surface, effectiveness factor and significance of external and internal heat and mass transport are shown in Figure A.1-A.2 in Appendix. It is observed that internal

mass transport is reaction rate controlling at temperatures above 500 °C and up to 8 atm while intrinsic kinetics are controlling the system at temperature below 400 °C. The external mass transport resistance is at the examined conditions never strong enough to be identified as controlling the observed TOF. However, the effects of external mass transport resistance can be seen at high temperature and total pressure, and would conceptually be controlling the reaction rate at more extreme conditions. For other reaction conditions a combination of kinetics, external and internal mass transport controls the reaction rate of complete methane oxidation over Pd/Al_2O_3.

4.2 Multiscale reactor modelling

In Paper II, the full reactor model outlined in section 3.1 is used to evaluate the effects on total pressure of complete methane oxidation though a monolith Pd/Al_2O_3 reactor. The development aims to take a step towards the systems which are used in applications. The effects of total pressure on the methane conversion are investigated as well as internal gradients in the axial direction of the monolith reactor. The studied bulk gas composition contains 1000 vol.-ppm CH_4, 10 vol.-% O_2, 10 vol.-% H_2O and 5 vol.-% CO_2. In contrast to Paper I, porous structure is assumed to inhibit a predominantly mesoporous and macroporous structure and Knudsen diffusion is hence omitted from the Bosanquet correlation. The relative importances of Knudsen diffusion and molecular diffusion have been studied by others from both a theoretical and experimental perspectives [61–66]. In a mesoporous structure the molecular diffusion has a strong affect on the effective diffusivity, while in a microporous structure the Knudsen diffusion should be considered for a correct estimate of the effective diffusion coefficient.

The inlet gas flow is set to 1500 mL/min, over a monolith having a length of 15 mm and diameter of 12 mm. The palladium loading of the catalyst is set to 1 wt.-% with a palladium dispersion of 25%. The simulated methane conversions for total pressures of 1, 2, 4 and 10 atm are shown in Figure 4.3. Increasing the total pressure results in a delayed ignition of the reaction but displays an increased conversion at higher temperatures. The temperatures at which 20 % conversion is achieved are 402, 406, 412 and 421 °C for a total pressure of 1, 2, 4 and 10 atm, respectively. The increased ignition temperature for increased total pressures is explained by the increased coverage of bicarbonates, adsorbed water and hydroxyl groups as discussed in Paper I. The in-

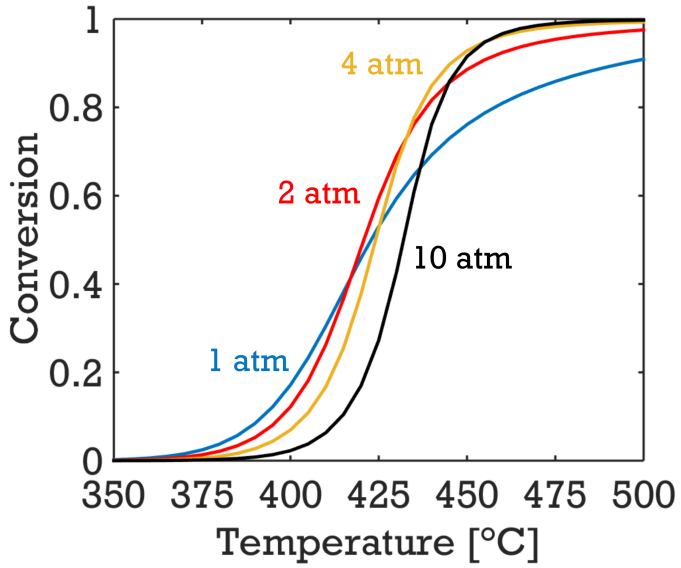

Figure 4.3: Simulated methane conversion profiles over the Pd/Al2O3 catalyst at total pressures of 1 (blue), 2 (red), 4 (yellow) and 10 (black) atm for a gas composition of 1000 vol.-ppm CH_4, 10 vol.-% O_2, 10 vol.-% H_2O and 5 vol.-% CO_2.

creased coverage reduces the availability of free Pd-O site pairs where the methane can dissociatively adsorb. A more complex effect of the total pressure is observed at the intermediate temperatures of 420-445 °C. Here the methane conversion first increases when the total pressure is raised from 1 to 2 and 4 atm but is observed to decrease when the total pressure reaches 10 atm. The method of degree of rate control is used to analyze the surface kinetics for an inlet gas composition and varying temperatures and total pressures. The rate control for dissociative methane adsorption (solid lines), decomposition of CH_3 (crossed lines), water desorption (triangles) and water decomposition into hydrogen and hydroxyl (dotted lines) are shown in Figure 4.4. The degree of rate control analysis shows that the dissociative methane adsorption is the most rate controlling step while methyl decomposition or water desorption is the second most controlling step, depending on the reaction conditions. The decomposition of water into hydrogen and hydroxyl displays a negative rate control, meaning a negative effect on the overall activity, for all conditions except for high total pressures and low temperatures. The negative rate control is probably due to the high total pressures and thus a strong competition for the active sites. For every decomposed water molecule, the leaving hydrogen atom bonds to an undercoordinated oxygen atom and therefore reducing the availability of free Pd-O sites even further. Since the availability of active

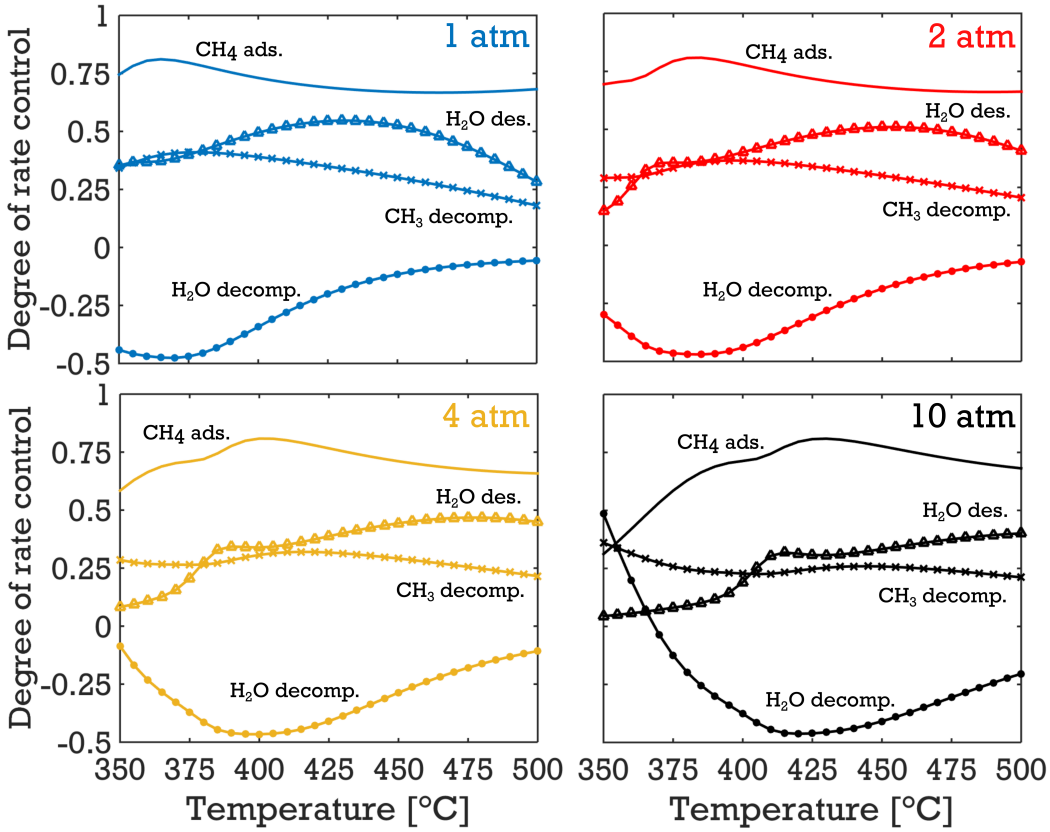

Figure 4.4: The degree of rate control for dissociative methane adsorption (solid lines), decomposition of CH_3 (crossed lines), water desorption (triangles) and water decomposition into hydrogen and hydroxyl (dotted lines) over Pd/Al_2O_3 at total pressures of 1 atm (blue), 2 atm (red), 4 atm (yellow) and 10 atm (black) and varying temperatures.

sites is low to begin with, even less methane can adsorb dissociatively and hence a negative rate control is observed. Interestingly, the rate control for water decomposition shows a positive value at high total pressures and low temperatures. This is assumed to be due to a slight difference in the reaction pathway in how methane adsorbs and how C-H dissociation occurs. Here at the lowest temperatures, methane adsorption and the C-H dissociation are preferred on surface hydroxyl groups, i.e. an alternative pathway is made possible which is also discussed by another study [58]. The explanation is further motivated by the fact that the rate control of water decomposition is correlated to the coverage of hydroxyl groups where a lower hydroxyl coverage correlates to a higher degree of rate control. The reason that a positive rate control is seen at 10 atm but not at lower total pressures, is because the TOF is so low that the positive effect of increased hydroxyl coverage overcomes the negative effects from the loss of active sites

from the adsorbed hydrogen on undercoordinated oxygen. This complexity arises from the fact that high total pressures are used in the study, resulting in a high competing adsorption. A similar rate control would probably not be observed if total pressures of millibars would be used.

Mass and heat transport effects were evaluated, as in Paper I, by comparing the time constants fo external and internal mass and heat transport, and reaction. For the examined inlet gas conditions it is concluded that the observed reaction rate of methane oxidation in a porous alumina supported palladium catalyst is controlled by surface kinetics below 415 °C at a total pressure of 1 and 2 atm. For total pressures of 4 and 10 atm the surface kinetics are controlling the observed reaction rate at temperatures lower than 420 and 430 °C, respectively. At higher temperatures the observed reaction rate is not controlled by a single phenomenon but influenced by a mixture of surface kinetics, external and internal mass transport. However, the significance of mass transport increases with increasing total pressure in the mixed control region. The significances of external and internal mass transport are shown in Appendix A.3.

The gradients and the effects of total pressure through the monolith are assessed at three different temperatures, namely at 390, 425 and 480 °C and for 1, 2, 4 and 10 atm and shown in Figure 4.5. The methane conversion for the lowest and highest temperature at 1 atm is 8 and 89 %, respectively. The temperature of 425 °C is chosen due to the more complex dependency of total pressure on methane conversion where the conversion first increases with total pressure but then decreases at the highest total pressures. The rows in Figure 4.5, from top to bottom, show the average reaction rate, bulk gas (diamonds) and catalyst surface temperature (solid line) and the effectiveness factor, respectively, for 1 (blue), 2 (red), 4 (yellow) and 10 atm (black). The columns in Figure 4.5, from left to right, show the situation for 390, 425 and 480 °C, respectively. For 390 °C, the axial gradients are observed to be insignificant and increasing the total pressure results in decreased reaction rate, as previously discussed and shown in Paper I. At 480 °C the average reaction rate is much faster since methane dissociate easier which results in more exothermic heat being released. The increased surface temperature has a positive effect on the reaction rate according to the Arrhenius expression. An observed effect is a strongly decreasing reaction rate in the axial direction of the monolith due to the decreasing methane concentration. Even though the reaction rate increases with increasing total pressure the effects of mass transport become more ap-

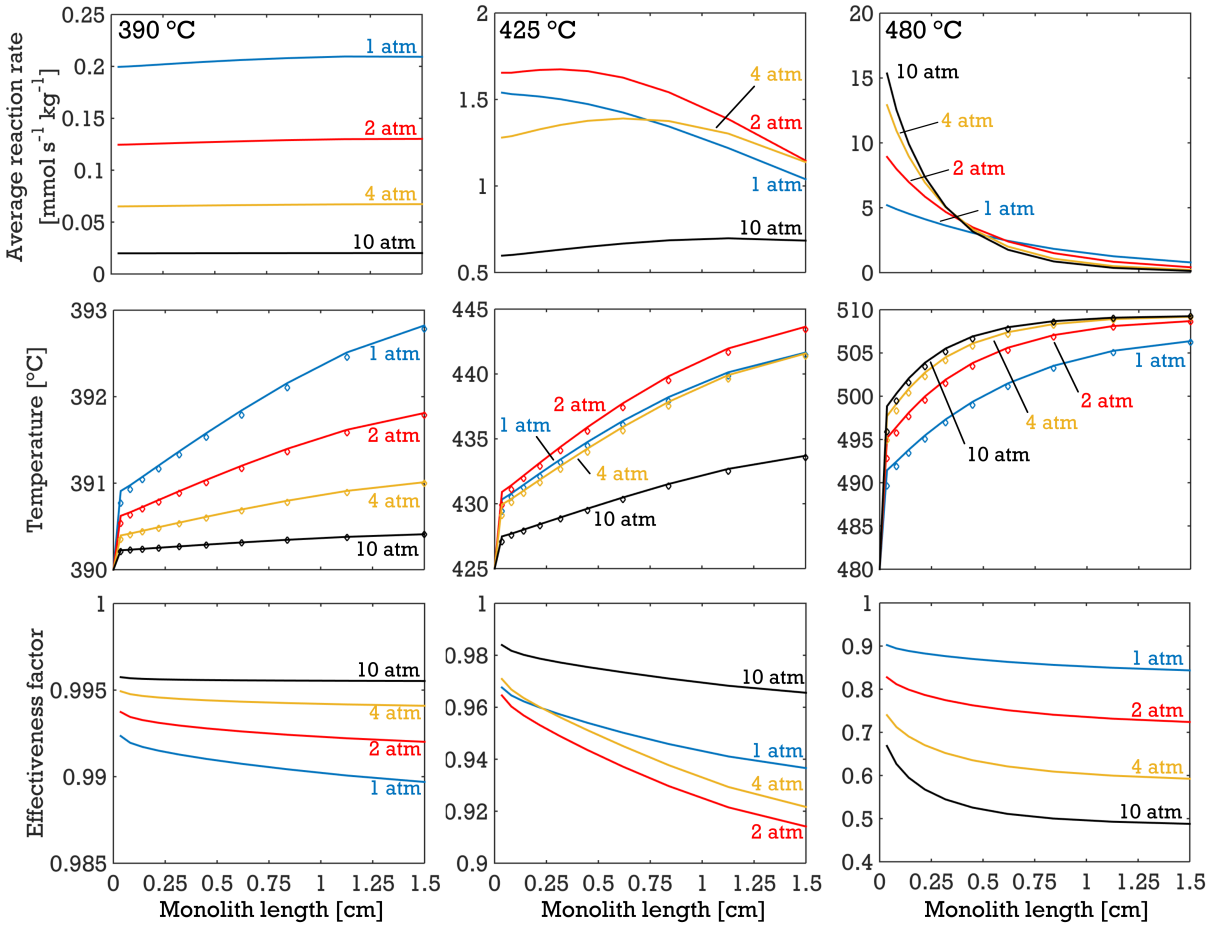

Figure 4.5: The axial variations of average reaction rate, catalyst (solid line) and bulk gas temperature (diamonds) and effectiveness factor in a monolith Pd/Al_2O_3 reactor for methane oxidation at total pressures of 1 atm (blue), 2 (red), 4 (yellow) and 10 atm (black). Left column: 390 °C. Middle column: 425 °C. Right column: 480 °C .

parent. A high reaction rate creates steeper gradients inside the porous catalyst and a faster molecular transport becomes more important to effectively use the entire catalyst. The latter can be understood from the effectiveness factor. Thus the monolith contains palladium oxide that is not used to its full potential and a higher turnover frequency is possible for the sites furthest into the porous catalyst. Hence, the importance of reactor design and cost optimisation is visualised. At 425 °C an interesting trend is observed where the reaction rate at first increases with increasing total pressures up to 2 atm but drops again at total pressures of 4 and 10 atm. The effect can be regarded as a transition between the low- and high-temperature effects. At total pressures up to 2 atm the porous catalyst can still withstand the increased presence of bicarbonates, adsorbed wa-

ter and hydroxyl groups originating from the carbon dioxide and water in the bulk gas while maintaining a relatively high reaction rate. When the total pressure is increased to 4 atm the increased amount of surface bicarbonates and adsorbed water begins to inhibit the dissociation of methane, hence slowing down the reaction rate. The effects are severe at 10 atm with a strong negative effect on the overall conversion (see Figure 4.3).

4.3 Design and construction of pressurized experimental setup

Modelling is a valuable tool to understand and explain reaction kinetics and reaction mechanisms. However, a model must be validated by experiments to become reliable. A pressurized experimental setup has therefore been constructed which includes a DRIFTS (Diffusive Reflectance Infrared Spectroscopy) reaction cell and a monolith reactor. The former will be used to characterize the surface species and their coverages during reaction, which the multiscale model outputs as a result. The monolith reactor will be used to analyse the kinetics of the complete methane oxidation reaction by performing activity measurements and correlate the results to the multiscale model. The combination offers many possibilities to validate the model in detail.

Chapter 5

Concluding remarks

This work has aimed to investigate the total pressure effects on the activity of Pd/Al_2O_3 for complete methane oxidation from a modelling perspective. The mutiscale model developed in this work is based on kinetics obtained from first-principles calculations in terms of density functional theory and transition state theory. The multiscale model considers a 2D monolith reactor with axial and radial gradients to evaluate the methane conversion as well as external and internal transport phenomena. The examined gas was a representative exhaust gas composition from combustion of methane in natural gas and biogas containing 1000 vol.-ppm CH_4, 10 vol.-% O_2, 10 vol.-% H_2O and 5 vol.-% CO_2. The exhaust gas was examined for temperatures and total pressures between 325-625 °C and 1-10 atm, respectively. It was revealed by the model that for a simulated exhaust gas composition an increased total pressure can significantly enhance the reaction rate in a monolith coated with Pd/Al_2O_3, and hence the conversion, of methane at temperatures above 420 °C. The positive effect was shown to be highly temperature dependent at the examined inlet gas conditions due to a high hindering effect of surface species. At temperatures below 420 °C the active sites of Pd/Al_2O_3 are blocked by hindering surface species and display a negative total pressure dependence. The hindering surface species were identified to be bicarbonates, adsorbed water and hydroxyl groups which originate from the high concentrations of carbon dioxide and water in the bulk gas. A temperature of around 420 °C is required to overcome the desorption barriers of bicarbonate and adsorbed water and obtain a relatively clean catalyst surface where methane can dissociate freely on the palladium oxide. The observed reaction rate at the examined conditions were found to be controlled by surface kinetics for temperatures below 415 °C while a combination of kinetics, external and internal mass transport is to

be expected above the same temperature and up to the highest examined temperature of 500 °C for the monolith rector. The increased mass transport significance results in a drastically lower effectiveness factor which highlights the importance of catalyst design. A degree of rate control analysis revealed that the most controlling reaction step is the dissociative methane adsorption for all combinations of temperature and total pressure. It is only at the lowest temperature and highest total pressure that decomposition of adsorbed water into hydroxyl and hydrogen is more controlling. The second most controlling reaction step is the desorption of water and decomposition of methyl groups. The rate control of the former reaction step decreaes at lower temperatures when the total pressure increased.

Finally, this study has developed a comprehensive multiscale model where the geometry can be varied in order to optimize the catalyst design for complete methane oxidation on palladium oxide in ambient and pressurized conditions. The multiscale model stretches the common modelling boundaries and paves the way for further modelling and experimental studies to identify the bottleneck of complete methane oxidation in the quest for high performing catalyst.

Acknowledgements

The research presented in this thesis was carried out at the Division of Applied Chemistry and the Competence Centre for Catalysis (KCK), Chalmers University of Technology, Göteborg, Sweden during the period October 2015 to September 2018.

The Competence Centre for Catalysis is hosted by Chalmers University of Technology and financially supported by the Swedish Energy Agency and the member companies AB Volvo, ECAPS AB, Johnson Matthey AB, Preem AB, Scania CV AB, Umicore AG & Co. KG and Volvo Car Corporation AB. Additional support has been obtained from Chalmerska forskningsfonden and the computational time has been granted by SNIC at C3SE (Göteborg).

I would also like to thank:

My main supervisor Magnus Skoglundh, for all the guidance and support. I highly appreciate that you take your time and that your door is always open whenever I have questions. Thank you for all the feedback regarding posters, presentation, manuscripts and abstracts. It has helped me in developing my skills within the field of research.

My co-supervisors Per-Anders Carlsson, Derek Creaser and Henrik Grönbeck for all your feedback and input. Thanks for our fruitful discussions which has helped me understand how we see catalysis from different perspectives which has raised the level of this work.

Hanna Härelind, Frida Andersson, Lotta Pettersson and Ann Jakobsson for the administrative help and the well-organised and fun events.

Lasse Urholm, Lennart Norberg and Ulf Stenman for all the laughs but especially all your help in the reactor rooms.

My office mate Johanna Englund for your positive attitude and the working atmosphere that we have. For helping me stay positive when things bunch up or don't go as planned.

Looking forward for many more hours of discussions while listening to good, bad and strange music. By the way, I still think we disturb our neighbouring offices when you are in charge of the music volume.

My current and past colleges at KCK and TYK for the amazing working environment we have and for all the fun we have had together both within the corridors of Chalmers and outside of work. Special thanks goes to: Adam, Alvaro, Andreas, Anna, Chris, Colin, David, Emma, Felix, Giulio, Ida, Johan, Leo, Linda, Maria, Mattias, Maxime, Mikael, Mikkel, Milene, Mo, Natalia, Peter, Saba, Sam, Simone, Ting.

A very special thanks goes to my mother, father and brother who has always encouraged and supported me over the years. Without you this would not have been possible.

Carl-Robert Florén, Göteborg, August, 2018

Bibliography

[1] The World Bank. Population, total. Retrieved 2018-08-15, https://data.worldbank.org/indicator/SP.POP.TOTL.

[2] The World Bank. Population growth (annual %). Retrieved 2018-08-15, https://data.worldbank.org/indicator/SP.POP.GROW?end=2017&start=1960.

[3] Working Group III Technical Support Unit. Climate change 2014 mitigation of climate change. Technical report, The Intergovernmental Panel on Climate Change (IPCC), 2014.

[4] IEA. Co_2 emissions from fuel combustion 2017 overview. Technical report, 2017.

[5] UNFCCC. Kyoto protocol to the united nations framework convention on climate change, 1998.

[6] European Commision. Europe 2020 - a european strategy for smart, sustainable and inclusive growth, 2010.

[7] IPCC. *Climate Change 2007: The Physical Science Basis. Contribution of Working Group I to the Fourth Assessment*, chapter 2, pages 129–235. Cambridge University Press, 2007.

[8] EPA. Inventory of u.s greenhouse gas emissions and sinks, 2018.

[9] Climate change 1995, the science of climate change: Summary for policymakers and technical summary of the working group i report. Technical report, The Intergovernmental Panel on Climate Change (IPCC), 1995.

[10] Izzet Karakurt, Gokhan Aydin, and Kerim Aydiner. Sources and mitigation of methane emissions by sectors: A critical review. *Renewable Energy*, 39(1):40 – 48, 2012.

[11] Rafiu O. Yusuf, Zainura Z. Noor, Ahmad H. Abba, Mohd Ariffin Abu Hassan, and Mohd Fadhil Mohd Din. Methane emission by sectors: A comprehensive review

of emission sources and mitigation methods. *Renewable and Sustainable Energy Reviews*, 16(7):5059 – 5070, 2012.

[12] M. Gambino, R. Cericola, P. Corbo, and S. Iannaccone. Carbonyl compounds and pah emissions from cng heavy-duty engine. *Journal of Engineering for Gas Turbines and Power*, 115(4):747–749, 1993.

[13] Diesel fuels technical review. Technical report, Chevron, 2007.

[14] S. Faramawy, T. Zaki, and A.A.-E. Sakr. Natural gas origin, composition, and processing: A review. *Journal of Natural Gas Science and Engineering*, 34:34 – 54, 2016.

[15] Paul Boehm and Tarek Saba. Identification of natural gas sources using geochemical forensic tools. Retrieved 2018-07-23, http://announce.exponent.com/practice/environmental/ef/EF_Notes_Vol_5.pdf, 2009.

[16] Union Gas. Chemical composition of natural gas. Retrieved 2018-07-23, https://www.uniongas.com/about-us/about-natural-gas/chemical-composition-of-natural-gas, 2018.

[17] A. Molino, F. Nanna, Y. Ding, B. Bikson, and G. Braccio. Biomethane production by anaerobic digestion of organic waste. *Fuel*, 103:1003 – 1009, 2013.

[18] IEA Bioenergy Task 40 and Task 37. Biomethane status and factors affecting market development and trade. Technical report, IEA, 2014.

[19] Green Gas Grids. Biomethane. Retrieved 2018-07-23, http://www.greengasgrids.eu/about/biomethane.html.

[20] Gavin Towler and Ray Sinnott. *Chemical Engineering Design*. Butterworth-Heinemann, Boston, second edition edition, 2012.

[21] Mohammad Nurunnabi, Yuya Mukainakano, Shigeru Kado, Tomohisa Miyazawa, Kazu Okumura, Toshihiro Miyao, Shuichi Naito, Kimihito Suzuki, Ken-Ichiro Fujimoto, Kimio Kunimori, and Keiichi Tomishige. Oxidative steam reforming of methane under atmospheric and pressurized conditions over Pd/NiO-MgO solid solution catalysts. *Applied Catalysis A: General*, 308:1–12, jul 2006.

[22] Michael Reinke, John Mantzaras, Rolf Schaeren, Rolf Bombach, Andreas Inauen, and Sabine Schenker. High-pressure catalytic combustion of methane over platinum: In situ experiments and detailed numerical predictions. *Combustion and Flame*, 136(1-2):217–240, 2004.

[23] A. Di Benedetto, G. Landi, V. Di Sarli, P. S. Barbato, R. Pirone, and G. Russo. Methane catalytic combustion under pressure. *Catalysis Today*, 197(1):206–213, 2012.

[24] A. Di Benedetto, P. S. Barbato, and G. Landi. Effect of CO 2 on the Methane Combustion over a Perovskyte Catalyst at High Pressure. *Energy & Fuels*, 27(10):6017–6023, 2013.

[25] Artem A. Slepterev, Valerii S. Salnikov, Pavel G. Tsyrulnikov, Aleksandr S. Noskov, Viktor N. Tomilov, Nataliya A. Chumakova, and Andrey N. Zagoruiko. Homogeneous high-temperature oxidation of methane. *Reaction Kinetics and Catalysis Letters*, 91(2):273–282, Sep 2007.

[26] Patrick Gélin and Michel Primet. Complete oxidation of methane at low temperature over noble metal based catalysts: A review. *Applied Catalysis B: Environmental*, 39(1):1–37, 2002.

[27] Zhenhua Li and Gar B Hoflund. A review on complete oxidation of methane at low temperatures. *Journal of Natural Gas Chemistry*, 12:153–160, 2003.

[28] Yuxuan Xin, Hai Wang, and Chung K. Law. Kinetics of catalytic oxidation of methane, ethane and propane over palladium oxide. *Combustion and Flame*, 161(4):1048–1054, 2014.

[29] Sheedeh Fouladvand, Stefan Schernich, Jörg Libuda, Henrik Grönbeck, Torben Pingel, Eva Olsson, Magnus Skoglundh, and Per Anders Carlsson. Methane oxidation over Pd supported on ceria-alumina under rich/lean cycling conditions. *Topics in Catalysis*, 56(1-8):410–415, 2013.

[30] Per Anders Carlsson, Erik Fridell, and Magnus Skoglundh. Methane oxidation over pt/al2o3 and pd/al2o3 catalysts under transient conditions. *Catalysis Letters*, 115(1-2):1–7, 2007.

[31] Martin Schmal, Mariana M V M Souza, Violeta Virginia Alegre, Mônica Antunes Pereira da Silva, Deborah Vargas César, and Carlos A C Perez. Methane oxidation - effect of support, precursor and pretreatment conditions - in situ reaction XPS and DRIFT. *Catalysis Today*, 118(3):392–401, 2006.

[32] James B. Miller and Manaswita Malatpure. Pd catalysts for total oxidation of methane: Support effects. *Applied Catalysis A: General*, 495:54–62, 2015.

[33] Koshi Sekizawa, Hardiyanto Widjaja, Shingo Maeda, Yasushi Ozawa, and Koichi Eguchi. Low temperature oxidation of methane over Pd catalyst supported on

metal oxides. *Catalysis Today*, 59(1-2):69–74, 2000.

[34] Koichi Eguchi and Hiromichi Arai. Low temperature oxidation of methane over pd-based catalysts—effect of support oxide on the combustion activity. *Applied Catalysis A: General*, 222(1-2):359–367, 2001.

[35] Ryuji Kikuchi, Shingo Maeda, Kazunari Sasaki, Stefan Wennerström, Yasushi Ozawa, and Koichi Eguchi. Catalytic activity of oxide-supported pd catalysts on a honeycomb for low-temperature methane oxidation. *Applied Catalysis A: General*, 239(1):169 – 179, 2003.

[36] Jason F. Weaver, Can Hakanoglu, Jeffery M. Hawkins, and Aravind Asthagiri. Molecular adsorption of small alkanes on a pdo(101) thin film: Evidence of σ-complex formation. *The Journal of Chemical Physics*, 132(2):024709, 2010.

[37] A. Hellman, A. Resta, N. M. Martin, J. Gustafson, A. Trinchero, P.-A. Carlsson, O. Balmes, R. Felici, R. van Rijn, J. W. M. Frenken, J. N. Andersen, E. Lundgren, and H. Grönbeck. The active phase of palladium during methane oxidation. *The Journal of Physical Chemistry Letters*, 3(6):678–682, 2012. PMID: 26286272.

[38] Abbin Antony, Aravind Asthagiri, and Jason F. Weaver. Pathways and kinetics of methane and ethane c–h bond cleavage on pdo(101). *The Journal of Chemical Physics*, 139(10):104702, 2013.

[39] Adriana Trinchero, Anders Hellman, and Henrik Grönbeck. Metal oxide sites for facile methane dissociation. *physica status solidi (RRL) - Rapid Research Letters*, 8(6):605–609, 6 2014.

[40] Natalia M. Martin, Maxime Van den Bossche, Anders Hellman, Henrik Grönbeck, Can Hakanoglu, Johan Gustafson, Sara Blomberg, Niclas Johansson, Zhi Liu, Stephanus Axnanda, Jason F. Weaver, and Edvin Lundgren. Intrinsic ligand effect governing the catalytic activity of pd oxide thin films. *ACS Catalysis*, 4(10):3330–3334, 2014.

[41] M. Van Den Bossche. *Methane oxidation over palladium oxide: From electronic structure to catalytic conversion*. PhD thesis, Chalmers University of Technology, 2017.

[42] Ryuji Kikuchi, Shingo Maeda, Kazunari Sasaki, Stefan Wennerström, and Koichi Eguchi. Low-temperature methane oxidation over oxide-supported pd catalysts: inhibitory effect of water vapor. *Applied Catalysis A: General*, 232(1):23 – 28, 2002.

[43] Dragos Ciuparu, Nikolaos Katsikis, and Lisa Pfefferle. Temperature and time dependence of the water inhibition effect on supported palladium catalyst for methane combustion. *Applied Catalysis A: General*, 216(1):209 – 215, 2001.

[44] Sara Colussi, Fabrizio Arosio, Tania Montanari, Guido Busca, Gianpiero Groppi, and Alessandro Trovarelli. Study of sulfur poisoning on pd/al2o3 and pd/ceo2/al2o3 methane combustion catalysts. *Catalysis Today*, 155(1):59 – 65, 2010. IWCC7 andfutureconceptsinenergy-relatedcatalysis.

[45] J. B. Anderson. A criterion for isothermal behavior of a catalyst pellet. *Chemical Engineering Science*, 18:147–148, 1963.

[46] Kostas C. Metaxas and Nikos G. Papayannakos. Studying the internal mass transfer phenomena inside a ni/al2o3 catalyst for benzene hydrogenation. *Chemical Engineering Journal*, 140(1):352 – 357, 2008.

[47] Alpay Şahin, Erdem Alp, Demet Eserci, and H. Canan Cabbar. Effective diffusion constant and adsorption constant of synthesized alumina, zirconia, and alumina–zirconia composite material. *Chemical Engineering Communications*, 204(10):1129–1142, 2017.

[48] Tronconi Enrico and Forzatti Pio. Adequacy of lumped parameter models for scr reactors with monolith structure. *AIChE Journal*, 38(2):201–210, 1992.

[49] R. Hawthorne. *AIChE Symp. Ser.*, 70:428, 1974.

[50] Enrico Fermi. Statistical method to determine some properties of atoms. *Rend. Accad. Naz. Lincei*, 6:602–607, 1927.

[51] L. H. Thomas. The calculation of atomic fields. *Mathematical Proceedings of the Cambridge Philosophical Society*, 23(5):542–548, 1927.

[52] P. Hohenberg and W. Kohn. Inhomogeneous electron gas. *Phys. Rev.*, 136:B864–B871, Nov 1964.

[53] W. Kohn and L. J. Sham. Self-consistent equations including exchange and correlation effects. *Phys. Rev.*, 140:A1133–A1138, Nov 1965.

[54] Takao Tsuneda. *Exchange-Correlation Functionals*, pages 101–124. Springer Japan, Tokyo, 2014.

[55] Henry Eyring. The activated complex in chemical reactions. *The Journal of Chemical Physics*, 3(2):107–115, 1935.

[56] M. G. Evans and M. Polanyi. Some applications of the transition state method to the calculation of reaction velocities, especially in solution. *Trans. Faraday Soc.*,

31:875–894, 1935.

[57] Mikkel Jørgensen and Henrik Grönbeck. Connection between macroscopic kinetic measurables and the degree of rate control. *Catal. Sci. Technol.*, 7:4034–4040, 2017.

[58] Maxime Van Den Bossche and Henrik Grönbeck. Methane Oxidation over PdO(101) Revealed by First-Principles Kinetic Modeling. *Journal of the American Chemical Society*, 137(37):12035–12044, 2015.

[59] R Burch, F Urbano, and P Loader. Methane combustion over palladium catalysts: The effect of carbon dioxide and water on activity. *Applied Catalysis A: General*, 123(1):173–184, 1995.

[60] F. H Ribeiro, M Chow, and R. A Dalla Betta. Kinetics of the Complete Oxidation of Methane over Supported Palladium Catalysts. *Journal of Catalysis*, 146(2):537–544, 1994.

[61] V. Novák, F. Štěpánek, P. Kočí, M. Marek, and M. Kubíček. Evaluation of local pore sizes and transport properties in porous catalysts. *Chemical Engineering Science*, 65(7):2352–2360, 2010.

[62] Vladimír Novák, Petr Kočí, Miloš Marek, František Štěpánek, Patricia Blanco-García, and Glenn Jones. Multi-scale modelling and measurements of diffusion through porous catalytic coatings: An application to exhaust gas oxidation. *Catalysis Today*, 188(1):62–69, 2012.

[63] Vladimír Novák, Petr Kočí, Tomáš Gregor, Jae Soon Choi, František Štěpánek, and Miloš Marek. Effect of cavities and cracks on diffusivity in coated catalyst layer. *Catalysis Today*, 216:142–149, 2013.

[64] P. Kočí, F. Štěpánek, M. Kubíček, and M. Marek. Modelling of micro/nano-scale concentration and temperature gradients in porous supported catalysts. *Chemical Engineering Science*, 62(18-20):5380–5385, 2007.

[65] Petr Kočí, Vladimír Novák, František Štěpánek, Miloš Marek, and Milan Kubíček. Multi-scale modelling of reaction and transport in porous catalysts. *Chemical Engineering Science*, 65(1):412–419, 2010.

[66] Michal Dudák, Vladimír Novák, Petr Kočí, Miloš Marek, Patricia Blanco-García, and Glenn Jones. Prediction of diffusivity and conversion of n-decane and CO in coated Pt/γ-Al2O3catalyst depending on porous layer morphology. *Applied Catalysis B: Environmental*, 150-151:446–458, 2014.

Appendix

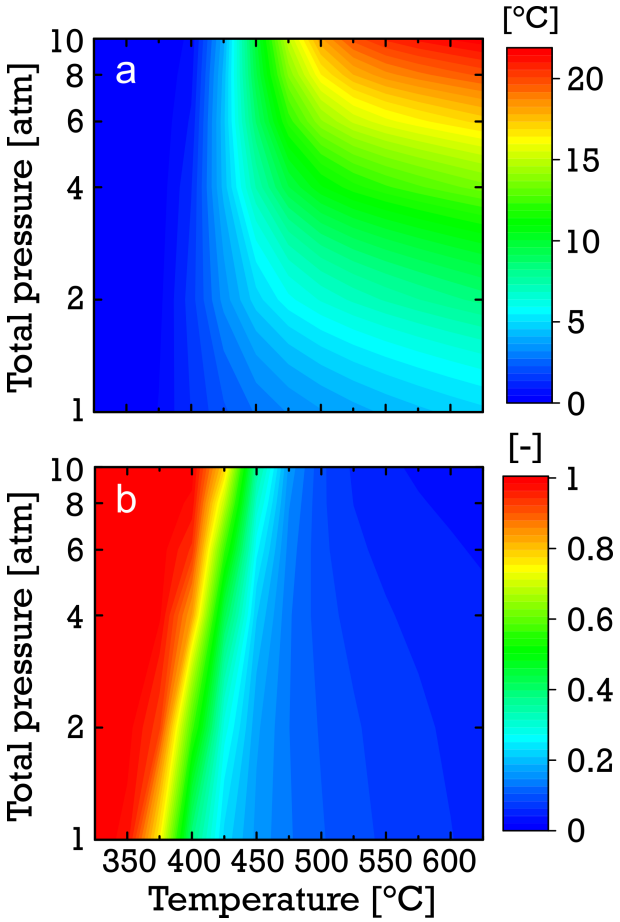

Figure A.1: Surface to gas temperature difference (Ts–Tg) (a) and effectiveness factor (b) for complete CH_4 oxidation on PdO at varying total pressure and temperature.

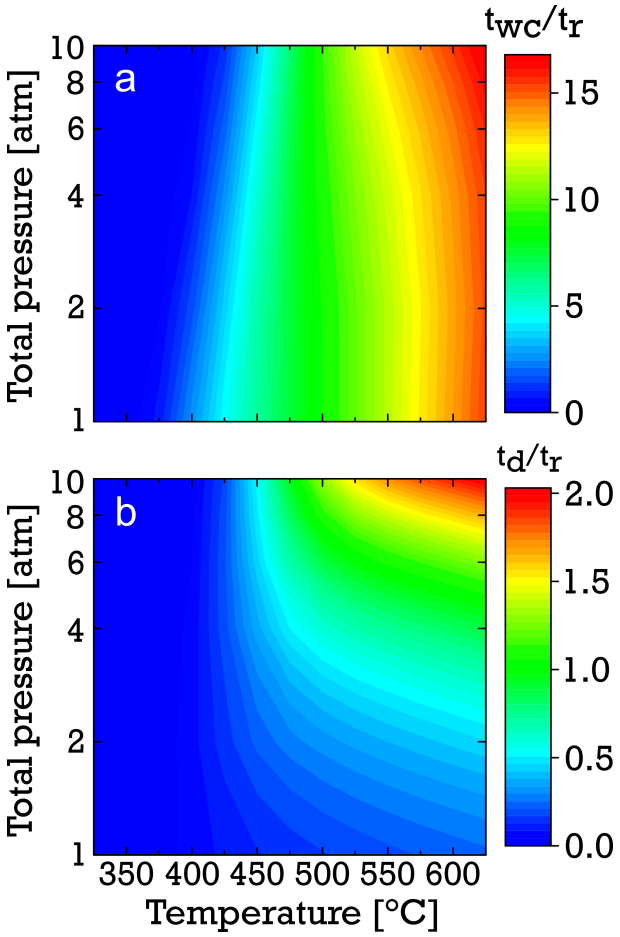

Figure A.2: The ratio of internal diffusion time and reaction time for internal (twc/tr) (a) and external (td/tr) (b) mass transport for complete CH_4 oxidation on PdO at varying total pressure and temperature.

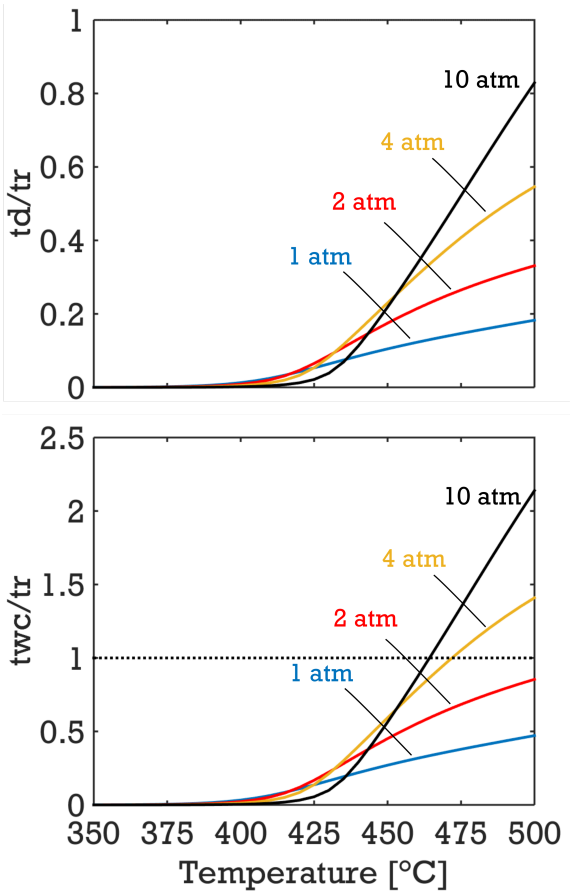

Figure A.3: The external (a) and internal (b) mass transport significance, here taken as the weighted average over all tanks, at total pressures of 1 atm (blue), 2 atm (red), 4 atm (yellow) and 10 atm (black) and varying temperatures.

Table A.1: Kinetic parameters for the considered elementary steps including carbonaceous intermediates. f and and b denote forward and backward reactions, respectively. The values for the pre-exponential factors (1/s) are calculated at 700 K and 1 bar. The energy barriers are given in eV. Reactants adsorbed on Pd and O sites are in regular and bold font, respectively. Activation energies denoted with * correspond to the barrier for diffusion of the reactants, as the actual reaction is non-activated.

no.	Reaction equation			A_f	A_b	$E_{a,f}^{HSE06}$	$E_{a,b}^{HSE06}$
(1)	CH_4(g) + S_1-**S_2**	⇄	CH_3-**H**	7.6×10^{4}	1.8×10^{14}	0.29	1.32
(2)	CH_4(g) + OH + S_1	⇄	CH_3 + H_2O	2.8×10^{4}	1.4×10^{13}	0.30	1.08
(3)	CH_4(g) + OH-**H** + S_1	⇄	CH_3 + H_2O + **H**	”	”	0.24	0.62
(4)	CH_4(g) + OH + S_1 + **H**	⇄	CH_3-**H** + H_2O	”	”	0.04	1.32
(5)	CH_4(g) + OH-**H** + S_1 + **H**	⇄	CH_3-**H** + H_2O + **H**	”	”	0.69	1.62
(6)	CH_4(g) + O	⇄	CH_3 + OH	6.7×10^{4}	7.7×10^{13}	0.33	1.77
(7)	CH_4(g) + O_2	⇄	CH_3 + OOH	—	—	2.26	—
(8)	CH_3-**H** + OH	⇄	CH_2-**H** + H_2O	3.6×10^{12}	8.3×10^{13}	1.14	1.15
(9)	CH_3-**H** + OH-**H**	⇄	CH_2-**H** + H_2O + **H**	”	”	2.08	1.03
(10)	CH_3-**H** + O	⇄	CH_2OH-**H** + S_1	1.1×10^{13}	1.0×10^{15}	0.73	2.37
(11)	CH_3-**H**	⇄	S_1 + CH_3(g) + **H**	1.0×10^{16}	2.6×10^{7}	2.74	0.00
(12)	CH_3 + OH	⇄	CH_2 + H_2O	3.6×10^{12}	8.3×10^{13}	0.83	1.14
(13)	CH_3 + OH-**H**	⇄	CH_2 + H_2O + **H**	”	”	1.16	0.84
(14)	CH_3 + O	⇄	CH_2OH + S_1	1.1×10^{13}	1.0×10^{15}	0.47	3.31
(15)	CH_3 + O_2	⇄	CH_3OO + S_1	—	—	1.11	—
(16)	CH_3 + **S_2**	⇄	CH_2-**H**	7.9×10^{12}	1.5×10^{14}	1.29	1.71
(17)	CH_3 + **S_2**	⇄	S_1 + **CH_3**	4.6×10^{13}	1.0×10^{15}	1.15	2.09
(18)	CH_3-**Vac** + **S_2**	⇄	CH_2-**H** + **Vac**	”	”	1.44	1.34
(19)	CH_3	⇄	S_1 + CH_3(g)	1.0×10^{16}	2.6×10^{7}	1.54	0.00
(20)	**CH_3** + O	⇄	**CH_2** + OH	3.9×10^{13}	7.5×10^{13}	0.194*	3.30
(21)	**CH_3** + OH	⇄	**CH_2** + H_2O	4.9×10^{13}	4.0×10^{13}	0.291*	2.25
(22)	**CH_3** + OH-**H**	⇄	**CH_2** + H_2O + **H**	”	”	1.15	2.38
(23)	**CH_3**	⇄	**S_2** + CH_3(g)	1.9×10^{17}	2.6×10^{7}	1.96	0.00
(24)	CH_2-**H** + OH	⇄	CH_2OH-**H** + S_1	1.1×10^{13}	8.6×10^{13}	0.31	1.29
(25)	CH_2-**H** + OH-**H**	⇄	CH_2OH-**H** + **H** + S_1	”	”	1.11	1.03
(26)	CH_2-**H** + **S_2**	⇄	**CH_2** + **H**	3.7×10^{13}	1.2×10^{14}	1.29	2.15
(27)	CH_2 + OH	⇄	CH_2OH + S_1	1.1×10^{13}	8.6×10^{13}	0.06	1.94
(28)	CH_2 + OH-**H**	⇄	CH_2OH + **H** + S_1	”	”	0.19	1.01
(29)	CH_2 + O_2	⇄	CH_2OO + S_1	—	—	0.79	—
(30)	CH_2 + **S_2**	⇄	CH-**H**	1.1×10^{14}	1.3×10^{14}	1.23	1.63
(31)	CH_2 + **S_2**	⇄	**CH_2** + S_1	3.7×10^{13}	1.2×10^{14}	0.22	1.97
(32)	**CH_2** + S_1	⇄	CH_2O-**Vac**	5.5×10^{13}	1.2×10^{12}	0.82	0.22
(33)	CH_2OH + **S_2**	⇄	CH_2O-**H**	5.4×10^{13}	1.5×10^{12}	0.21	0.52
(34)	CH_2O + **S_2**	⇄	CHO-**H**	8.8×10^{12}	2.8×10^{14}	0.69	2.19
(35)	CH_2O + OH	⇄	CHO + H_2O	1.5×10^{13}	1.0×10^{14}	0.52	2.01
(36)	CH_2O + OH-**H**	⇄	CHO + H_2O + **H**	”	”	0.37	0.80
(37)	CH_2O	⇄	S_1 + CH_2O(g)	4.8×10^{15}	1.8×10^{7}	0.55	0.00
(38)	CH + **S_2**	⇄	C-**H**	3.5×10^{13}	6.0×10^{13}	1.31	1.42
(39)	CH + **S_2**	⇄	CHO + **Vac**	6.1×10^{12}	5.3×10^{12}	0.32	2.17
(40)	CHO-**H** + OH	⇄	CO + **H** + H_2O	2.1×10^{14}	3.2×10^{13}	0.33	0.00
(41)	CHO + **S_2**	⇄	CO + **H**	3.9×10^{14}	2.8×10^{14}	0.78	2.44
(42)	CHO + **S_2**	⇄	S_1 + **CHO**	4.5×10^{13}	5.2×10^{13}	0.71	1.19
(43)	CHO + OH	⇄	CO + H_2O	2.1×10^{14}	3.2×10^{13}	0.58	2.88
(44)	**CHO** + S_1	⇄	CO_2(g) + H + **Vac**	9.2×10^{12}		1.08	
(45)	**CHO** + OH	⇄	CO(g) + H_2O	1.8×10^{14}		0.291*	
(46)	**CHO** + S_1	⇄	CHOO-**Vac**	1.3×10^{13}	4.3×10^{12}	0.12	0.09
(47)	CHOO-**Vac** + **S_2**	⇄	CO_2(g) + S_1 + **Vac** + **H**	4.4×10^{14}		1.41	
(48)	CHOO + **S_2**	⇄	CO_2(g) + S_1 + **H**	3.2×10^{14}		1.83	
(49)	CHOO + OH	⇄	CO_2(g) + H_2O + S_1	4.4×10^{14}		1.95	
(50)	CO	⇄	S_1 + CO(g)	7.7×10^{15}	1.9×10^{7}	1.40	0.00
(51)	CO + **S_2**	⇄	S_1 + **CO**	4.7×10^{12}	7.8×10^{12}	0.45	0.07
(52)	**CO** + S_1	⇄	CO_2-**Vac**	8.1×10^{12}	2.1×10^{12}	0.41	0.84
(53)	CO_2-**Vac**	⇄	S_1 + CO_2(g) + **Vac**	1.9×10^{14}	1.5×10^{7}	0.69	0.00
(54)	CO + O	⇄	CO_2(g) + 2 S_1	2.3×10^{13}		0.194*	
(55)	CO + O_2	⇄	O + CO_2(g) + S_1	5.7×10^{12}		1.51	
(56)	CO + OH	⇄	HOCO + S_1	1.1×10^{13}	6.3×10^{13}	0.32	0.53
(57)	HOCO + **S_2**	⇄	CO_2(g) + S_1 + **H**	1.5×10^{14}		0.22	

Table A.2: Kinetic parameters for the considered elementary steps including carbon dioxide, carbonates and bicarbonates. f and and b denote forward and backward reactions, respectively. The values for the pre-exponential factors (1/s) are calculated at 700 K and 1 bar. The energy barriers are given in eV.

no.	Reaction equation			A_f	A_b	$E_{a,f}^{HSE06}$	$E_{a,b}^{HSE06}$
(58)	S_1 + CO_2(g)	⇄	CO_2	1.5×10^{7}	8.4×10^{15}	0.00	0.52
(59)	CO_2 + O	⇄	CO_3 + S_1	1.0×10^{13}	1.0×10^{13}	0.23	0.80
(60)	CO_2 + OH	⇄	CO_3H_A + S_1	”	”	0.25	0.46
(61)	CO_3H_A	⇄	CO_3H_B	”	”	0.87	1.56

Table A.3: Kinetic parameters for the considered elementary steps including O_xH_y intermediates. f and and b denote forward and backward reactions, respectively. The values for the pre-exponential factors (1/s) are calculated at 700 K and 1 bar. The energy barriers are given in eV. Reactants adsorbed on Pd and O sites are in regular and bold font, respectively. Activation energies denoted with * correspond to the barrier for diffusion of the reactants, as the actual reaction is non-activated.

no.	Reaction equation			A_f	A_b	$E_{a,f}^{HSE06}$	$E_{a,b}^{HSE06}$
(62)	H_2O	⇄	S_1 + H_2O(g)	3.6×10^{15}	2.3×10^{7}	1.38	0.00
(63)	H_2O-OH	⇄	OH + S_1 + H_2O(g)	”	”	1.73	0.00
(64)	H_2O-(OH-**H**)	⇄	OH-**H** + S_1 + H_2O(g)	”	”	1.88	0.00
(65)	H_2O + $\mathbf{S}_2$	⇄	OH-**H**	1.3×10^{13}	6.3×10^{13}	0.13	0.23
(66)	H_2O-OH + $\mathbf{S}_2$	⇄	OH-**H** + OH	”	”	0.59	0.09
(67)	H_2O-(OH-**H**) + $\mathbf{S}_2$	⇄	2 OH-**H**	”	”	0.54	0.04
(68)	O_2(g) + S_1	⇄	O_2	1.8×10^{7}	9.9×10^{15}	0.00	0.58
(69)	O_2 + S_1	⇄	2 O	3.0×10^{13}	2.8×10^{13}	2.01	0.42
(70)	O_2(g) + Vac	⇄	**O**	1.8×10^{7}	2.2×10^{16}	0.00	1.71
(71)	**O** + S_1	⇄	O + $\mathbf{S}_2$	2.7×10^{13}	2.0×10^{13}	1.16	1.17
(72)	O + **Vac**	⇄	S_1 + $\mathbf{S}_2$	2.3×10^{13}	6.1×10^{13}	0.194*	2.93
(73)	O_2 + **Vac**	⇄	O + $\mathbf{S}_2$	1.3×10^{16}	1.1×10^{14}	0.73	1.87
(74)	OH	⇄	S_1 + OH(g)	2.8×10^{16}	2.4×10^{7}	2.26	0.00
(75)	OH-**H**	⇄	S_1 + OH(g) + **H**	”	”	3.37	0.00
(76)	H_2O(g) + O + S_1	⇄	2 OH	2.3×10^{7}	8.3×10^{15}	0.00	1.67
(77)	**H** + S_1	⇄	OH + **Vac**	6.7×10^{13}	1.5×10^{13}	1.43	0.294*
(78)	**H** + S_1	⇄	H + $\mathbf{S}_2$	2.3×10^{14}	3.2×10^{13}	1.93	0.83
(79)	H-**H**	⇄	H_2 + $\mathbf{S}_2$	1.6×10^{14}	1.3×10^{13}	1.49	0.29
(80)	H_2	⇄	S_1 + H_2(g)	4.6×10^{14}	7.0×10^{7}	0.63	0.00